

Does magnetic field impact tidal dynamics inside the convective zone of low-mass stars along their evolution?

A. Astoul, S. Mathis, C. Baruteau, F. Gallet, Antoine Strugarek, K. C. Augustson, A. S. Brun, E. Bolmont

▶ **To cite this version:**

A. Astoul, S. Mathis, C. Baruteau, F. Gallet, Antoine Strugarek, et al.. Does magnetic field impact tidal dynamics inside the convective zone of low-mass stars along their evolution?. Astronomy and Astrophysics - A&A, 2019, 631, pp.A111. 10.1051/0004-6361/201936477 . cea-02350013

HAL Id: cea-02350013
https://cea.hal.science/cea-02350013

Submitted on 5 Nov 2019

HAL is a multi-disciplinary open access archive for the deposit and dissemination of scientific research documents, whether they are published or not. The documents may come from teaching and research institutions in France or abroad, or from public or private research centers.

L'archive ouverte pluridisciplinaire **HAL**, est destinée au dépôt et à la diffusion de documents scientifiques de niveau recherche, publiés ou non, émanant des établissements d'enseignement et de recherche français ou étrangers, des laboratoires publics ou privés.

A&A 631, A111 (2019)
https://doi.org/10.1051/0004-6361/201936477
© A. Astoul et al. 2019

Astronomy & Astrophysics

Does magnetic field impact tidal dynamics inside the convective zone of low-mass stars along their evolution?

A. Astoul[1], S. Mathis[1], C. Baruteau[2], F. Gallet[3], A. Strugarek[1], K. C. Augustson[1], A. S. Brun[1], and E. Bolmont[4]

[1] AIM, CEA, CNRS, Université Paris-Saclay, Université Paris Diderot, Sorbonne Paris Cité, 91191 Gif-sur-Yvette, France
e-mail: aurelie.astoul@cea.fr
[2] IRAP, Observatoire Midi-Pyrénées, Université de Toulouse, 14 avenue Edouard Belin, 31400 Toulouse, France
[3] Univ. Grenoble Alpes, CNRS, IPAG, 38000 Grenoble, France
[4] Observatoire de Genève, Université de Genève, 51 chemin des Maillettes, 1290 Sauverny, Switzerland

Received 7 August 2019 / Accepted 21 September 2019

ABSTRACT

Context. The dissipation of the kinetic energy of wave-like tidal flows within the convective envelope of low-mass stars is one of the key physical mechanisms that shapes the orbital and rotational dynamics of short-period exoplanetary systems. Although low-mass stars are magnetically active objects, the question of how the star's magnetic field impacts large-scale tidal flows and the excitation, propagation and dissipation of tidal waves still remains open.
Aims. Our goal is to investigate the impact of stellar magnetism on the forcing of tidal waves, and their propagation and dissipation in the convective envelope of low-mass stars as they evolve.
Methods. We have estimated the amplitude of the magnetic contribution to the forcing and dissipation of tidally induced magneto-inertial waves throughout the structural and rotational evolution of low-mass stars (from M to F-type). For this purpose, we have used detailed grids of rotating stellar models computed with the stellar evolution code STAREVOL. The amplitude of dynamo-generated magnetic fields is estimated via physical scaling laws at the base and the top of the convective envelope.
Results. We find that the large-scale magnetic field of the star has little influence on the excitation of tidal waves in the case of nearly-circular orbits and coplanar hot-Jupiter planetary systems, but that it has a major impact on the way waves are dissipated. Our results therefore indicate that a full magneto-hydrodynamical treatment of the propagation and dissipation of tidal waves is needed to properly assess the impact of star-planet tidal interactions throughout the evolutionary history of low-mass stars hosting short-period massive planets.

Key words. magnetohydrodynamics (MHD) – waves – planet-star interactions – stars: evolution – stars: magnetic field – stars: rotation

1. Introduction

Over the last two decades, a large variety of exoplanetary systems has been discovered, primarily through photometric transit and radial velocity observations (e.g. Perryman 2018). Among these systems, several populations of exoplanets orbit very close to their host stars (with orbital periods of a few days), such as hot-Jupiters, super-Earths, and mini-Neptunes (Mayor et al. 1997; Schlichting 2014). In these short period systems as well as in tight binary stars, tides induced by each other's body drive the rotational and orbital evolutions of the system through dissipation mechanisms (the so-called tidal dissipation, see e.g. Zahn 1977; Hut 1980; Zahn & Bouchet 1989; Goldreich & Nicholson 1989; Witte & Savonije 2002).

Usually, tides are split into two components following the work of Zahn (1966a,b,c, 1975, 1977). First, the equilibrium tide is the quasi-hydrostatic response of the main body to tidal perturbations induced by the companion. It is materialised by a large-scale deformation in the perturbed body, that is displayed as a near-equatorial tidal bulge in the direction of the companion. In addition, waves are excited in its interior as the equilibrium tide is not an exact solution to the equations of motion, providing an additional driving force (Ogilvie 2014). The tidally-forced waves correspond to the dynamical tides. The convective zone (CZ) of a perturbed rotating body is the seat of inertial waves that get dissipated by turbulent friction (e.g. Ogilvie & Lin 2004, 2007), while the radiative zone supports gravito-inertial waves which are dissipated by thermal damping and turbulent friction (e.g. Zahn 1975; Terquem et al. 1998; Goodman & Dickson 1998; Barker & Ogilvie 2010).

The dissipation of the dynamical tides in the CZ is very efficient in young stars (pre-main sequence and early main sequence) whereas for older stars the dissipation of the equilibrium tide dominates mainly because of the slower stellar rotation, as demonstrated for instance by Bolmont & Mathis (2016) (see also Strugarek et al. 2017; Gallet et al. 2017; Beck et al. 2018). The efficiency of the tidal excitation and viscous dissipation of inertial and gravito-inertial waves can be measured with the tidal quality factor Q. This quantity reflects the fact that the perturbed body undergoes a forced oscillation and dissipates a fraction of the associated energy during each oscillation period. It has been evaluated by Ogilvie & Lin (2004, 2007), with and without differential rotation (see also Guenel et al. 2016a,b, for this particular topic), in the case of giant planets and solar-type stars. Recently, Mathis (2015) and Gallet et al. (2017) explored the influence of mass, age and rotation based on the frequency-averaged dissipation estimates of Ogilvie (2013) to understand the behaviour of tidal dissipation along the evolution of stars. They emphasised that the variation of these parameters could drastically modify the strength of tidal dissipation with a higher

Open Access article, published by EDP Sciences, under the terms of the Creative Commons Attribution License (http://creativecommons.org/licenses/by/4.0), which permits unrestricted use, distribution, and reproduction in any medium, provided the original work is properly cited.

frequency-averaged tidal dissipation for low-mass stars. Similarly, Bolmont et al. (2017) highlighted the importance of the stellar metallicity. Within this context, the variations of tidal dissipation along stellar evolution have a strong impact on the orbital architecture of compact planetary systems and the planet survival (Bolmont & Mathis 2016; Benbakoura et al. 2019).

In the aforementioned studies of star-planet tidal interactions, an important ingredient is missing though: stellar magnetism. In the Sun and solar-like stars, magnetism is revealed by external magnetic features such as sunspots, prominences or flares (Donati & Landstreet 2009). The magnetic fields of solar-like stars originates from a powerful dynamo mechanism, sustained by turbulent convection and differential rotation in the convective envelope of the star (Brun & Browning 2017). Recent endeavours have been carried out to assess the effects of magnetism on tidally-excited inertial waves in stars (Wei 2016, 2018; Lin & Ogilvie 2018). In the presence of a magnetic field, tidal waves excited in the CZ become magneto-inertial waves. Moreover, they feel the magnetic tension of the large-scale magnetic field which affects their propagation and dissipation (Finlay 2008). These magnetically modified inertial waves have a broader range of propagation frequencies, compared to the hydrodynamical case, and can be dissipated through both viscous and Ohmic processes. Specifically, the transition between hydrodynamical and magneto-hydrodynamical (MHD) regimes have been explored in a shearing box model with a uniform magnetic field (Wei 2016) and in spherical geometry with both a uniform field directed along the z-axis and a dipolar magnetic field (Lin & Ogilvie 2018). The authors of these studies both stressed that the Lehnert number Le (Lehnert 1954) determines how important magnetism is to tidal dissipation. This dimensionless number compares the Alfvén velocity to the rotation speed of the body. Additionally, how magnetism influences the effective tidal force to excite magneto-inertial waves remains to be addressed, as mentioned in Lin & Ogilvie (2018, Appendix B). In practice, given the equation of motion tidal waves are excited by an effective body force driven by the Coriolis acceleration of the equilibrium tidal flow in the non-magnetised case (Ogilvie 2005). In the presence of a magnetic field, the Lorentz force acting on the equilibrium tide is likely to play a role in the excitation of tidal waves. Thus, this motivates the study of the impact of stellar magnetism on both dissipation and excitation of dynamical tides inside the CZ and along the evolution of low-mass stars.

The paper is organised as follows. In Sect. 2.1 we work out the contribution of magnetism to tidal forcing and derive a criterion to assess its importance relative to non-magnetised forces. This criterion features the Lehnert number and thus the magnetic field and the rotation speed of the body, as well as the tidal forcing frequency. Simple scaling laws are applied in Sect. 2.2 to estimate the dynamo-driven magnetic field in the convective envelope of low-mass stars. Thanks to the stellar evolution code STAREVOL (Sect. 2.3, see also Amard et al. 2019, and references therein), the strength of a mean magnetic field is given, in Sect. 2.4, at the base and top of the CZ for various low-mass stars. Thus, we evaluate in Sect. 2.5 the Lehnert number as a function of age, mass, initial rotation, and radius in the CZ of these stars. We then estimate in Sect. 2.6 the Lehnert number along with the rotation and tidal frequencies in several observed short-period exoplanetary systems to assess the importance of the star's magnetic field on the tidal forcing. Based on our estimates of the Lehnert number, we compare in Sect. 3 the relative importance of Ohmic over viscous dissipations of tidally induced magneto-inertial waves throughout the evolution of low-mass stars. In Sect. 4, we examine how small-scale magnetic fields impact tidal forcing. Finally, we present in Sect. 5 the conclusions and perspectives of this work.

2. The Lorentz force influence on tidal forcing

The purpose of this section is to quantify the contribution of the stellar magnetic field to the tidal excitation of magneto-inertial waves in the CZ of low-mass stars.

2.1. A criterion to settle the importance of magnetism

We aim for an approach as general as possible, yet we restrict our model adopting a solid-body rotation with an angular frequency Ω. In particular, we do not assume a specific geometry for the magnetic field. We linearise the momentum and induction equations to derive the magnitude of the magnetic tidal forcing (the effective tidal force arising from the Lorentz force) and compare it with the classical hydrodynamical tidal forcing. We introduce the self-gravitational potential Φ_0, as well as the gravitational potential perturbation Φ, and the external tidal potential Ψ (see e.g. Zahn 1966a; Ogilvie 2013). The continuity and entropy equations are as given in Zahn's paper, with the addition of Ohmic heating to the entropy equation. The momentum equation for tidal perturbations in the co-rotating frame can be written as:

$$\rho_0(\partial_t \boldsymbol{u} + 2\boldsymbol{\Omega}\times\boldsymbol{u}) = -\boldsymbol{\nabla} p + \rho_0 \boldsymbol{\nabla}(\Phi+\Psi) + \rho\boldsymbol{\nabla}\Phi_0 + \boldsymbol{F}_\nu + \boldsymbol{F}_\mathrm{L}, \quad (1)$$

where ρ_0 is the mean density and $\boldsymbol{u}$, p, and ρ are the perturbed velocity, pressure, and density, respectively. We include the volumetric viscous force $\boldsymbol{F}_\nu = \rho_0\nu\boldsymbol{\nabla}^2\boldsymbol{u}$, which represents the effective action of turbulent convection on tidal flows with ν the effective so-called eddy-viscosity (e.g. Zahn 1966b, 1989; Ogilvie & Lesur 2012; Mathis et al. 2016) which we assume to be constant in the CZ. Moreover,

$$\boldsymbol{F}_\mathrm{L} = \frac{\boldsymbol{\nabla}\times\boldsymbol{B}_0}{\mu_0}\times\boldsymbol{b} + \frac{\boldsymbol{\nabla}\times\boldsymbol{b}}{\mu_0}\times\boldsymbol{B}_0$$

is the linearised Lorentz force, where $\boldsymbol{B}_0$ and $\boldsymbol{b}$ are the large-scale and perturbed magnetic fields, respectively. Note also that we have no background flow ($\boldsymbol{u}_0 = 0$) as we work in the rotating frame, the action of the convective flows is parametrised as a diffusion, and any differential rotation and associated meridional flows are neglected. Furthermore, the linearised induction equation is:

$$\partial_t \boldsymbol{b} = \boldsymbol{\nabla}\times(\boldsymbol{u}\times\boldsymbol{B}_0) + \eta\boldsymbol{\nabla}^2\boldsymbol{b}, \quad (2)$$

with η the magnetic turbulent diffusivity, related to the eddy-viscosity by the relationship $\eta = \nu/\mathrm{Pm}$, where Pm is the turbulent magnetic Prandtl number often chosen close to unity (e.g. Camargo & Tasso 1992; Jurčišinová et al. 2013; Käpylä et al. 2019).

Following Ogilvie (2005, 2013), we decompose all physical perturbed quantities X into a non-wave like part associated with the equilibrium tide denoted as X_e, and a wave-like part X_d related to the dynamical tides. The equilibrium tidal flow $\boldsymbol{u}_\mathrm{e}$ is defined as the velocity resulting from the hydrostatic adjustment of the primary due to the perturbation induced by the companion in the rotating frame of the tidal bulge. This frame rotates at the corresponding tidal frequency $n\Omega_\mathrm{o}/2$ (see Remus et al. 2012), where n labels the temporal harmonic of the orbital motion of the perturber (when projecting the tidal potential on the spherical harmonics basis) and Ω_o is the associated orbital frequency.

In the adiabatic case, this hydrostatic equilibrium leads to (Zahn 1966a):

$$-\boldsymbol{\nabla} p_\mathrm{e} + \rho_0 \boldsymbol{\nabla}(\Phi_\mathrm{e} + \Psi) + \rho_\mathrm{e} \boldsymbol{\nabla}\Phi_0 = 0. \tag{3}$$

This equation comes from Eq. (1) without the left hand side and dissipative terms. As a first step, we also neglect the deformation of the stellar structure induced by rotation and magnetic field. In the case of magnetic fields this is a reasonable assumption except in the low density region near the stellar surface (Duez et al. 2010). For the centrifugal acceleration, this is a fair hypothesis for slow and median rotators while potentially strong deformation should be taken into account for young rapid rotators (see e.g. Gallet & Bouvier 2013, Fig. 7). We split the equation of induction in the co-rotating frame, accounting for the equilibrium and dynamical tides decomposition:

$$\begin{cases} \boldsymbol{b}_\mathrm{e} = \boldsymbol{\nabla} \times (\boldsymbol{\xi}_\mathrm{e} \times \boldsymbol{B}_0) & \text{(4a)} \\ \partial_\mathrm{t} \boldsymbol{b}_\mathrm{d} = \boldsymbol{\nabla} \times (\boldsymbol{u}_\mathrm{d} \times \boldsymbol{B}_0) + \eta \boldsymbol{\nabla}^2 \boldsymbol{b}_\mathrm{d}, & \text{(4b)} \end{cases}$$

where $\boldsymbol{\xi}_\mathrm{e}$ is the equilibrium tide displacement, defined by $\boldsymbol{u}_\mathrm{e} = \partial_\mathrm{t} \boldsymbol{\xi}_\mathrm{e}$, given a mean static magnetic field $\boldsymbol{B}_0$. We also introduce $\boldsymbol{u}_\mathrm{d}$, the perturbed flow of the dynamical tide. We assume here that $\boldsymbol{B}_0$ does not vary over the tidal timescale which is a few days. This is corroborated by the fact that the large-scale magnetic field varies very little (far below one order of magnitude) within several years for the majority of observed stars (Vidotto et al. 2014). Moreover, we choose to define the magnetic field associated with the equilibrium tide as the field it induces by the advection of $\boldsymbol{B}_0$. We neglect the Ohmic diffusion acting on the equilibrium tide because its time scale R^2/η, where R is the radius of the star which is also the length of variation of this flow, is much larger than its typical time of variation (in the range of a few days for Hot Jupiter), even when considering a turbulent magnetic diffusivity. One can not do the same assumption for dynamical tides since they involve potentially smaller length scales, for example along waves' attractors. The equation of induction for dynamical tides (Eq. (4b)) follows from this definition when writing the equation of induction for the sum of the equilibrium and dynamical tide perturbations (Eq. (2)) since it is a linear equation.

In the momentum equation, we use the Cowling approximation (Cowling 1941) for the dynamical tides i.e. we neglect their perturbed gravitational potential Φ_d. In addition, as our model applies to a convective region (i.e. adiabatically stratified), the term $\rho_\mathrm{d} \boldsymbol{\nabla}\Phi_0$ is neglected because it is related to the buoyancy force associated with gravity waves. Using Eq. (3), the momentum equation for tidally-forced magneto-inertial waves becomes:

$$\rho_0(\partial_\mathrm{t} \boldsymbol{u}_\mathrm{d} + 2\boldsymbol{\Omega} \times \boldsymbol{u}_\mathrm{d}) + \boldsymbol{\nabla} p_\mathrm{d} - \boldsymbol{F}_\nu(\boldsymbol{u}_\mathrm{d}) - \boldsymbol{F}_\mathrm{L}(\boldsymbol{b}_\mathrm{d}) = f(\boldsymbol{u}_\mathrm{e}), \tag{5}$$

where the wave-like part encompassing the propagation of tidal waves (on the left hand side of the equation), is excited by an effective force driven by the equilibrium tidal flow (on the right hand side). This force can be written as:

$$f(\boldsymbol{u}_\mathrm{e}) = \underbrace{-\rho_0(\partial_\mathrm{t} \boldsymbol{u}_\mathrm{e} + 2\boldsymbol{\Omega} \times \boldsymbol{u}_\mathrm{e})}_{f_\mathrm{hydro}} + \underbrace{\frac{\boldsymbol{\nabla} \times \boldsymbol{B}_0}{\mu_0} \times [\boldsymbol{\nabla} \times (\boldsymbol{\xi}_\mathrm{e} \times \boldsymbol{B}_0)] + \frac{\boldsymbol{\nabla} \times [\boldsymbol{\nabla} \times (\boldsymbol{\xi}_\mathrm{e} \times \boldsymbol{B}_0)]}{\mu_0} \times \boldsymbol{B}_0}_{f_\mathrm{mag}}.$$

It is worth noting that the action of turbulent friction on the hydrostatic flow has been neglected for the same reasons we ignored the ohmic diffusion in Eq. (4a). The term f_hydro comprises the driving inertial force and the Coriolis acceleration (see the Appendix B in Ogilvie 2005) while f_mag embodies the action of the Lorentz force on the hydrostatic displacement and has been derived by Lin & Ogilvie (2018, see Appendix B). These authors studied the propagation and dissipation of magneto-inertial waves excited by the effective forcing induced solely by the Coriolis acceleration of the equilibrium tide (in short $f(\boldsymbol{u}_\mathrm{e}) = f_\mathrm{hydro}$). However, they also suggest that a large-scale magnetic field can potentially interact with the equilibrium tide for sufficiently large Lehnert numbers (typically Le > 0.1). For this reason, we propose to examine the relative importance of both forcings f_mag and f_hydro. We use R as the typical length scale of the large-scale magnetic field and of the equilibrium tide, which involves large-scale flows. Henceforth, we can give the order of magnitude of the different forcings:

$$\begin{cases} f_\mathrm{hydro} \sim \rho_0 u_\mathrm{e} \sigma_\mathrm{max} & \text{with} \sigma_\mathrm{max} = \max[\sigma_\mathrm{t}, 2\Omega] \\ f_\mathrm{mag} \sim B_0^2 \xi_\mathrm{e}/(\mu_0 R^2) \end{cases},$$

and their ratio:

$$\frac{f_\mathrm{mag}}{f_\mathrm{hydro}} \simeq \frac{B_0^2}{\rho_0 \mu_0 (2\Omega R)^2} \times \frac{2\Omega \xi_\mathrm{e}}{u_\mathrm{e}} \times \frac{2\Omega}{\sigma_\mathrm{max}} \equiv \mathrm{Le}^2 \times \mathrm{Ro}_\mathrm{t}^{-1} \times \hat{\sigma}_\mathrm{max}^{-1}, \tag{6}$$

where we define the Lehnert number as $\mathrm{Le} = B_0/(\sqrt{\rho_0 \mu_0} 2\Omega R)$. We also introduce the Doppler-shifted tidal Rossby number $\mathrm{Ro}_\mathrm{t} = \sigma_\mathrm{t}/(2\Omega)$ with $\sigma_\mathrm{t} = u_\mathrm{e}/\xi_\mathrm{e}$ the related tidal frequency, and a dimensionless frequency ratio $\hat{\sigma}_\mathrm{max} = \sigma_\mathrm{max}/(2\Omega) = \max[\mathrm{Ro}_\mathrm{t}, 1]$. According to Eq. (6), magnetism needs to be taken into account in the tidal forcing whenever $\mathrm{Le}^2/(\mathrm{Ro}_\mathrm{t} \hat{\sigma}_\mathrm{max}) \gtrsim 1$.

2.2. Scaling laws to estimate stellar magnetic fields

The determination of the Lehnert number inside the convective envelope of low-mass stars requires knowledge of the internal magnetic field of these stars. However, we are currently only able to constrain the magnetic field of stars at their surface. Indeed, thanks to Zeeman-Doppler Imaging, one can reconstruct the topology and strength of large-scale, stellar magnetic fields (Donati et al. 2006, 2007).

Regarding the Sun, internal magnetic fields can be assessed indirectly from surface tracers like sunspots, as a manifestation of flux ropes emerging through the surface (Charbonneau 2013). This approach is based on the so-called interface dynamo theory where the magnetic field is generated by a convective dynamo and pumped into the tachocline (the interface between the radiative and convective zones), where it eventually becomes strong enough to be buoyantly unstable, rise through the convection zone, and emerge at the surface as sunspots (Spiegel & Zahn 1992; Charbonneau 2014; Brun & Browning 2017). This picture has been recently questioned, especially by Wright & Drake (2016) by studying fully convective stars. It is indeed possible that the spot-forming magnetic fields can be generated in the bulk (Strugarek et al. 2017) or in the shallow layers (Basu 2016) of the CZ instead of overshoot layers beneath the core-envelope interface. Through helioseismology, Gough & Thompson (1990) and Antia et al. (2000) have placed an upper bound of 30 T on the toroidal magnetic field strength at the base of the CZ. On the contrary, the mean magnetic field at the Sun's surface is significantly smaller, about a few Gauss ($\sim 10^{-4}$ T), even though sunspots are the seats of local intense magnetic fields (several tenths of a Tesla).

As far as younger or smaller stars than the Sun are concerned, Vidotto et al. (2014) gives an overview of known large-scale surface magnetic fields, that appear to vary from the globally weak fields of the order of the Gauss for solar-like stars to the strong

Table 1. Magnetic fields derived from simple balances (forces or energies) written in the second column.

Regime	Balance	Estimation of $B_{\rm dyn}$
Equipartition	ME = KE	$\sqrt{\mu_0 2\mathrm{KE}}$
Buoyancy dynamo	$\frac{\mathrm{ME}}{\mathrm{KE}} = \mathrm{Ro}^{-1/2}$	$\sqrt{\mu_0 2\mathrm{KE}/\mathrm{Ro}^{1/2}}$
Magnetostrophy	$\boldsymbol{F}_{\rm L} = 2\rho_0 \boldsymbol{\Omega} \times \boldsymbol{u}$	$\sqrt{\mu_0 2\mathrm{KE}/\mathrm{Ro}}$

Notes. Details of the calculations are given in the Appendix A. KE and ME are the kinetic and magnetic energy densities of the convective flow, respectively.

Tesla-strength fields of M dwarf and T Tauri stars. They establish a relationship between surface magnetic field and the convective Rossby number $\mathrm{Ro} = u_{\rm c}/(2\Omega l_{\rm c})$, where $u_{\rm c}$ and $l_{\rm c}$ are the convective velocity and length, respectively. This dimensionless quantity is generally calculated at half the mixing-length $\alpha H_{\rm p}/2$ (Landin et al. 2010; Gilliland 1986) above the base of the CZ, with $H_{\rm p}$ the pressure scale height and α the mixing-length theory coefficient.

Nonetheless, as indicated above, it is difficult to estimate the magnetic field inside stars. In this context, 3D global non-linear simulations (Strugarek et al. 2017; Emeriau-Viard & Brun 2017) and scaling relationships for stellar dynamos (Augustson et al. 2019, and references therein) can help us to estimate the internal magnetic field strength in the convective envelope of low-mass stars. Three scaling laws are described hereafter and the derivation of the related dynamo-induced magnetic field is detailed in Appendix A. We have:

– the (turbulent) equipartition, that is often used to give an averaged, rough estimate of the magnetic field's amplitude in the bulk of the CZ (Brun & Browning 2017). It assumes that the dynamo is efficient i.e. that the system is equally good at generating magnetic field as it is at generating flows. This balance is also used in moderately active plages at the solar surface, while in the active sunspots superequipartition (i.e. magnetic energy is greater than kinetic energy) can be fairly common (Donati & Landstreet 2009).

– the buoyancy dynamo regime, in which the Coriolis, buoyancy and Lorentz forces are taken to have the same order of magnitude assuming a low atomic magnetic Prandtl number, that is the ratio of atomic viscosity to magnetic diffusivity (Davidson 2013; Augustson et al. 2019). This assumption is well verified for fast rotating giant planets, young contracting stars like T-Tauri and rapidly-rotating low-mass stars (Christensen et al. 2009).

– the magnetostrophic regime, for which the force balance is realised between the Coriolis and Lorentz forces. This balance, also called magnetostrophy, gives an upper estimate of the magnetic field. The magnetostrophic regime generally gives fields in super-equipartition (Brun et al. 2015; Augustson et al. 2019).

We summarise in Table 1 the order of magnitude estimation of the magnetic field (named hereafter $B_{\rm dyn}$) within the convective envelope of a low-mass star as obtained by the three aforementioned scaling laws. These relationships involve the kinetic and magnetic energy densities of the convective flow $\mathrm{KE} = \rho u_{\rm c}^2/2$ and $\mathrm{ME} = B_{\rm dyn}^2/(2\mu_0)$ respectively, along with the convective Rossby number $\mathrm{Ro} = u_{\rm c}/(2\Omega l_{\rm c})$ at the base of the CZ.

The main objective of this paper is to determine and quantify the impact of a large-scale magnetic field on the excitation and dissipation of the dynamical tides. We still discuss in Sect. 4 to what extent the small-scale component of the stellar magnetic field can influence the tidal flows. To allow comparison with the amplitude of observed surface magnetic fields of low-mass stars, we extrapolate a large-scale, dipolar, surface magnetic field from the scaling laws at the base of the CZ (Table 1). First, we suppose that the dipolar component of the star's magnetic field at the base of the CZ is a fraction γ of the dynamo-induced magnetic field at that location:

$$B_{\rm dip}(r_{\rm base}) = \gamma B_{\rm dyn}(r_{\rm base}). \tag{7}$$

The factor γ encapsulates both the ratio of large-scale to small-scale magnetic fields (similarly to the filling factor in Reiners 2012; See et al. 2019) and the part of the total energy that is available in the dipolar component of the magnetic field.

Then, we infer the dipolar component of the surface magnetic field simply as:

$$B_{\rm dip}(r_{\rm top}) = (r_{\rm base}/R)^3 B_{\rm dip}(r_{\rm base}), \tag{8}$$

where R is the radius of the star, the subscripts "base" and "top" are the position inside the CZ, and "dip" and "dyn" refer to the dipolar and dynamo-induced magnetic fields, respectively. As the dipolar magnetic field at the surface of the Sun is well known, typically 4 G (DeRosa et al. 2012), γ can be estimated for the Sun by using Eqs. (7) and (8):

$$\gamma = \frac{B_{\rm dip,\odot}(r_{\rm top})}{B_{\rm dyn,\odot}(r_{\rm base})} \times \left(\frac{r_{\rm base,\odot}}{R_\odot}\right)^{-3}, \tag{9}$$

with $R_\odot$, $B_{\rm dyn,\odot}(r_{\rm base})$ and $r_{\rm base,\odot}$ obtained from the grid models of the STAREVOL evolution code (see the Sect. 2.3 below) for a 1 $M_\odot$ star of the age of the Sun. In the following we assume that γ in Eq. (7) is independent of the mass and the age of the star, and that it takes the Sun's current value as in Eq. (9). This is a strong assumption since γ is close to a filling factor that depends on the Rossby number and therefore on the angular frequency of the star (See et al. 2019). Nevertheless, refining the expression of this factor would not change the final conclusions of this paper which are robust to several orders of magnitude, as we see later. The factor γ however depends on the scaling law used to estimate $B_{\rm dyn,\odot}$.

Finally, the dipolar component of a star's surface magnetic field will be estimated as

$$B_{\rm dip}(r_{\rm top}) = \gamma (r_{\rm base}/R)^3 B_{\rm dyn}(r_{\rm base}). \tag{10}$$

2.3. The stellar evolution code STAREVOL

To estimate the magnetic field and then the Lehnert number in the convective envelope of low-mass stars of different ages via the scaling laws described in Sect. 2.2, we use the 1D stellar evolution code STAREVOL (Amard et al. 2019). Initial masses of the stars range from 0.4 to 1.4 $M_\odot$, given a solar metallicity $Z = 0.0134$ (Asplund et al. 2009), and a mixing length parameter $\alpha = 1.9730$. This latter is defined by the calibration of the standard solar model and used to model convective regions according to the mixing length theory. Basic input microphysics like the equation of state, nuclear reactions or opacities, are described in Amard et al. (2016) and Lagarde et al. (2012). The initial rotation periods are fixed using the calibration for fast (1.6 days), median (4.5 days) and slow (9 days) rotators from Amard et al. (2019). The rotation is assumed to be uniform inside the CZ but varies dramatically with stellar ages (Gallet & Bouvier 2013). As a result, the evolution of the surface angular velocity dictates that of the Lehnert number. During the first few Myr of the pre-main

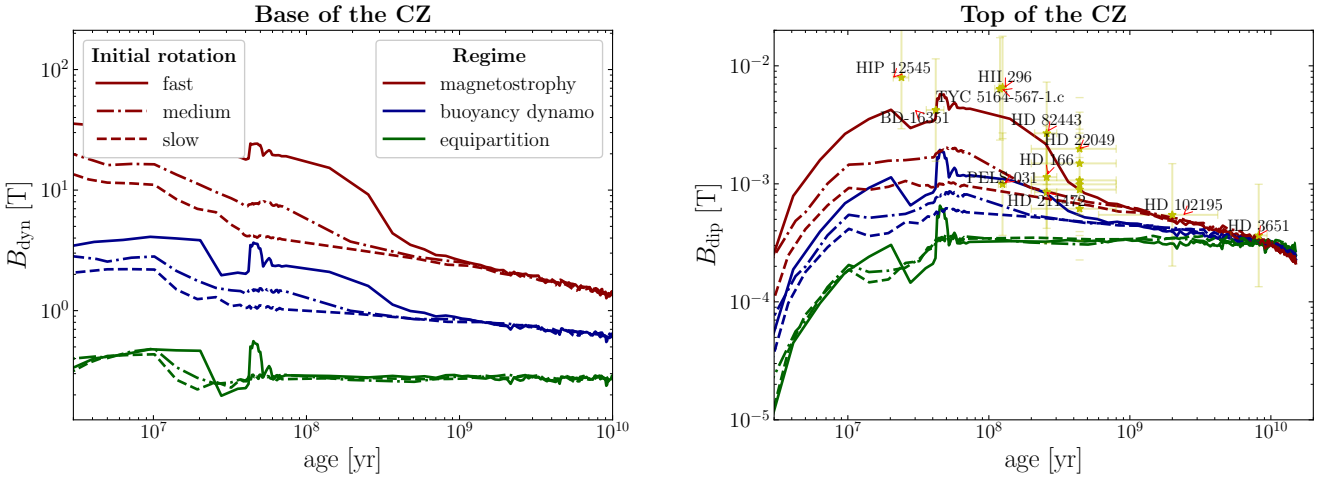


Fig. 1. Magnetic field versus the age of a 0.9 $M_\odot$ star for three different initial rotation periods. At the base of the CZ (*left panel*), the magnetic field is estimated from the scaling laws listed in Table 1. At the top of the CZ (*right panel*), the same scaling laws are used to extrapolate a dipolar magnetic field near the surface (see Eq. (10)). The "stars" symbols (★) that represent mean dipolar magnetic fields at the surface of 0.9 $M_\odot$ stars are taken from See et al. (2017), and the age of the stars are from Ge et al. (2006), Janson et al. (2008), Line et al. (2015), and Folsom et al. (2016). Multiple observations of the dipolar magnetic field of a star are joined by a line.

sequence (PMS), the surface angular velocity of the stars remains stationary as the result of star-disk magnetic interactions (Zanni & Ferreira 2013; Gallet & Bouvier 2015; Amard et al. 2016). This holds over the disk lifetime, typically a few Myr (Rebull et al. 2004; Bell et al. 2013; Gallet & Bouvier 2015). After the dissipation of the disk, the gravitational contraction of the star leads to an increase in the angular velocity, in order to conserve angular momentum, until the star begins hydrogen fusion at the zero-age main sequence (ZAMS). From this stage onward, magnetised stellar winds apply a torque on the star, spinning it down throughout its main sequence (MS) lifetime. In the STAREVOL code, the effects of a stellar wind acting from the early PMS to the tip of the MS are implemented using the prescription given by Matt et al. (2015). In the following, the base of the CZ refers to a height that is located $0.002R$ above the bottom of the CZ as computed in the STAREVOL model. This convention avoids erratic numerical behaviour of the mixing length convective velocity at the interface between the radiative and convective zones. Furthermore, the top of the CZ refers to the radius where the convective velocity vanishes in the STAREVOL models.

2.4. Estimation of the dipolar magnetic field at the base and the top of a CZ

Figure 1 shows the evolution of the magnetic field of a 0.9 $M_\odot$ star along its lifetime for the three different initial rotation rates stated in Sect. 2.3. It should be specified that we chose a 0.9 $M_\odot$ star rather than 1 $M_\odot$ to add measurements of the mean dipolar magnetic fields at the surface of stars in the early MS (see next paragraph). At the base of the CZ (left panel), the magnetic field is calculated with the scaling laws listed in Table 1. At the top of the CZ (right panel), we use these dynamo-induced magnetic fields to extrapolate dipolar magnetic fields near the surface by using Eq. (10). The results obtained with fast (1.6 days), median (4.5 days), and slow (9 days) initial rotations are plotted with solid, dash-dotted, and dashed curves, respectively. We note that the magnetic field decreases in time after about 50 Myr in the two panels for both the magnetostrophic and buoyancy dynamo regimes. It is due to the fact that these regimes depend on a positive power of the angular velocity (in the denominator of the Rossby number, see Table 1) that decreases after the ZAMS as a result of the stellar wind action on the star's surface. After 1 Gyr, this decline is well described by the empirical Skumanich relationship (Weber & Davis 1967; Skumanich 1972). At the age of the present Sun (~4.6 Gyr), the buoyancy dynamo and magnetostrophic regime at the base of the CZ give the order of magnitude of the toroidal magnetic field strength expected in the Sun at the tachocline, typically a few to a few tens of Tesla (Charbonneau 2013).

We have added on the plot for the top of the CZ (right-hand panel) the average unsigned measured dipolar field strength of 0.9 $M_\odot$ stars (See et al. 2017). We have adopted a conservative error estimate of 0.434 dex in $\log B_{\rm dip}$ for all stars. Note that HD 22049 displays several values of the amplitude of the dipolar magnetic field measured at different times. The ages of the stars and their errors are taken from Folsom et al. (2016) for the early MS stars and Ge et al. (2006), Janson et al. (2008), Line et al. (2015) for the three oldest stars. It is interesting to note that the strength of the observed dipolar magnetic fields seems to be steady for end PMS and early MS stars. This finding is consistent with the saturation levels observed by Vidotto et al. (2014), See et al. (2017) for the large-scale and dipolar surface magnetic fields at low Rossby numbers. As a matter of fact, low Rossby numbers means high angular frequencies and therefore stars in the vicinity of the ZAMS. However, whether or not this observed saturation level is an atmospheric effect or a dynamo related phenomenon has yet to be determined (Vilhu 1984; Jardine & Unruh 1999).

Dipolar fields of young stars seem to fit quite well with the magnetostrophic regime along with fast initial rotation. We must nevertheless specify that we realised the same plot with more observed dipolar magnetic fields (See et al., in prep., priv. comm.) featuring weaker magnetic fields for PMS and early MS stars, and so consistent with median and slow initial rotation. That being said, we have to bear in mind that several strong assumptions have been made to derive the dipolar magnetic field near the surface (Eq. (10), see also Appendix B). These prescriptions are nonetheless sufficient for this work given the robustness of our results as we see in Sect. 2.6.

We have plotted in Fig. 2 the ratio of the observed and estimated dipolar magnetic fields versus the mass of various

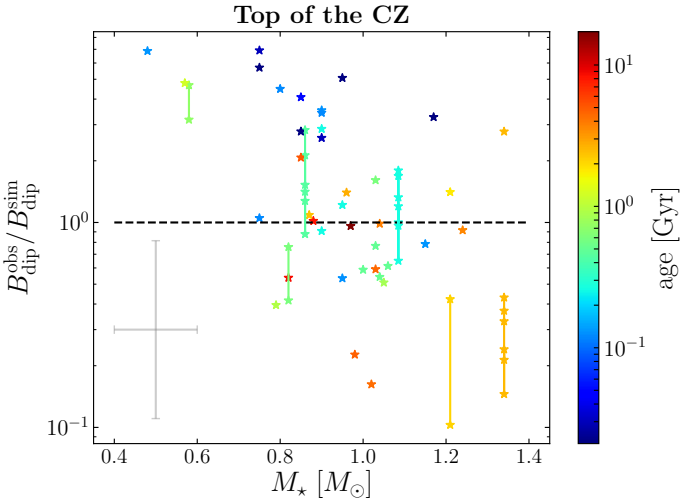


Fig. 2. Ratio of the mean unsigned observed dipolar magnetic field $B_{\rm dip}^{\rm obs}$ (See et al. 2017; Vidotto et al. 2014) over estimated dipolar magnetic field $B_{\rm dip}^{\rm sim}$ as a function of the mass of the star. The age of the stars is indicated in colour and ranges from 21 Myr to 17.2 Gyr. Magnetostrophic regime and median initial rotation have been used to plot the ratio $B_{\rm dip}^{\rm obs}/B_{\rm dip}^{\rm sim}$. Multiple observations of the dipolar magnetic field of a star are again joined by a line. A typical error bar for $M_\star$ and $B_{\rm dip}^{\rm obs}/B_{\rm dip}^{\rm sim}$ is indicated in grey. We have adopted a conservative error estimate of 0.434 dex in $\log B_{\rm dip}$ and 0.1 $M_\odot$ in $M_\star$.

low-mass stars distributed from PMS to MS stages. The magnetic field $B_{\rm sim}$ is calculated with the magnetostrophic regime and a median initial rotation. The magnetic field $B_{\rm obs}$ is again taken from See et al. (2017) and ages are from Vidotto et al. (2014) based on different methods (see the last quoted paper for more details). We note that the surface dipolar magnetic field of stars is well reproduced by $B_{\rm sim}$ within an order of magnitude. The estimate $B_{\rm dip}^{\rm sim}$ tends to deviate from $B_{\rm dip}^{\rm obs}$ for relatively massive ($M_\star \gtrsim 1.2\,M_\odot$) or very low-mass ($M_\star \lesssim 0.6\,M_\odot$) stars, which is not surprising considering that the ratio γ of dipolar/non dipolar magnetic field is determined from solar parameters (see Eq. (9)).

2.5. Lehnert number for a low-mass star along its evolution

Using the estimates of the dynamo-induced magnetic field in Table 1, we can express the related Lehnert number at the base of the CZ (see Table 2). Within each regime, Le depends on the convective Rossby number, and the ratio between the convective length scale and the stellar radius $l_{\rm c}/R$. This ratio results from the different length scales used in the magnetic scaling laws and in the definition of the Lehnert number (the length scales $l_{\rm c}$ and R respectively). Specifically, we choose a definition of the Lehnert number that is consistent with the previous works of Lin & Ogilvie (2018) and Wei (2018).

At the top of the CZ, we use the dipolar magnetic field derived in Eq. (10) to estimate the Lehnert number near the surface:

$$\mathrm{Le}_{\rm top} = \frac{B_{\rm dip}(r_{\rm top})}{\sqrt{\mu_0\rho_{\rm top}}2\Omega R} = \gamma\left(\frac{r_{\rm base}}{R}\right)^3\sqrt{\frac{\rho_{\rm base}}{\rho_{\rm top}}}\mathrm{Le}_{\rm base}, \tag{11}$$

where we recall that "top" and "base" refer to the position in the CZ and that $\mathrm{Le}_{\rm base}$ is taken from Table 2.

In Fig. 3, the Lehnert number squared of a 1 $M_\odot$ star is shown as a function of age, at the base (left panel, see Table 2) and top (right panel, Eq. (11)) of the CZ. The different scaling laws, with

Table 2. Lehnert number scaling laws depending on magnetic field regimes, detailed in Table 1.

Regime	Le scaling
Equipartition	$\mathrm{Ro}\times l_{\rm c}/R$
Magnetostrophy	$\sqrt{\mathrm{Ro}}\times l_{\rm c}/R$
Buoyancy dynamo	$\mathrm{Ro}^{3/4}\times l_{\rm c}/R$

fast and slow initial rotations, are shown with the same layout as Fig. 1. First, we note that Le^2 remains always smaller than unity, consistent with the previous works of Lin & Ogilvie (2018) and Wei (2018). Whether we look at the base or the top, Le^2 increases with decreasing initial rotation speed from the PMS until about 1 Gyr. This is the opposite behaviour to the magnetic field strength, since the Lehnert number decreases with the angular velocity (see Table 2 and Eq. (11)). Finally, Le^2 is greater at the base than at the top of the CZ as it scales with B^2.

The mass dependence of the Lehnert number is illustrated in Fig. 4, which displays Le^2 against age for stars ranging from 0.7 to 1.4 $M_\odot$. We have used slow initial rotation and the magnetostrophic regime to plot Le^2 at both the base and the top of the CZ. At the base of the CZ, we obtain the same features as in Fig. 3 i.e. Le^2 reaches a minimum at the ZAMS and increases during the MS. We highlight a quite small dispersion of the curves, though Le^2 still grows slightly with mass for $M_\star \lesssim 1.2\,M_\odot$ stars. This trend is driven mostly by the decay of the convective turnover time $\tau_{\rm c} = l_{\rm c}/u_{\rm c}$ when the mass grows (note that $\mathrm{Ro} = (\tau_{\rm c}2\Omega)^{-1}$ in Table 2). When $M_\star \gtrsim 1.2\,M_\odot$, the decrease in $l_{\rm c}/R$ at the base of the CZ for growing masses helps to reverse this behaviour. The drop in Le^2 with mass is even more pronounced at the top of the CZ for $M_\star \gtrsim 1\,M_\odot$. These changes simply reflects the fact that the convective envelope shrinks with mass, which naturally leads to an increase in convective length and a decrease in convective turnover time and density at the base of the CZ (see Table 2 and Eq. (11)).

2.6. The influence of magnetism on tidal forcing for observed star-planet systems

The ratio of the magnitude of the Lorentz forcing to the hydrodynamical forcing (Eq. (6)) does not only depend on the Lehnert number, but also on the Doppler-shifted Rossby number $\mathrm{Ro}_{\rm t}$ and the ratio of frequencies $\hat{\sigma}_{\rm max}$ which need to be estimated from a two-body system. Ogilvie (2014) gives the expression of the tidal frequency in the fluid frame, $\sigma_{\rm t}$ in our notations, using the integers l, m, n coming from the spherical harmonics functions on which the gravitational potential is projected (we refer the reader to Sect. 2.1 in Ogilvie 2014). The tidal frequency is $\sigma_{\rm t} = n\Omega_{\rm o} - m\Omega$, where m is the azimuthal order of the spherical harmonics, and n and $\Omega_{\rm o}$ have been introduced in Sect. 2.1. In the previous section, it has been shown that Le^2 does not go much beyond 10^{-3}, regardless of the age and the mass of the star at the base and top of the CZ (Figs. 3 and 4). This means that the ratio $f_{\rm mag}/f_{\rm hydro}$ (Eq. (6)) is likely to be small compared to unity, unless the rotation frequency is much greater (by at least a factor of a thousand) than the tidal frequency. Given the definition of the tidal frequency introduced above, the closer we get to a resonance between orbital and rotation frequencies, the more important the ratio $f_{\rm mag}/f_{\rm hydro}$ will be.

For the sake of simplicity we consider here systems with an almost circular and coplanar orbit. This allows us to reduce the

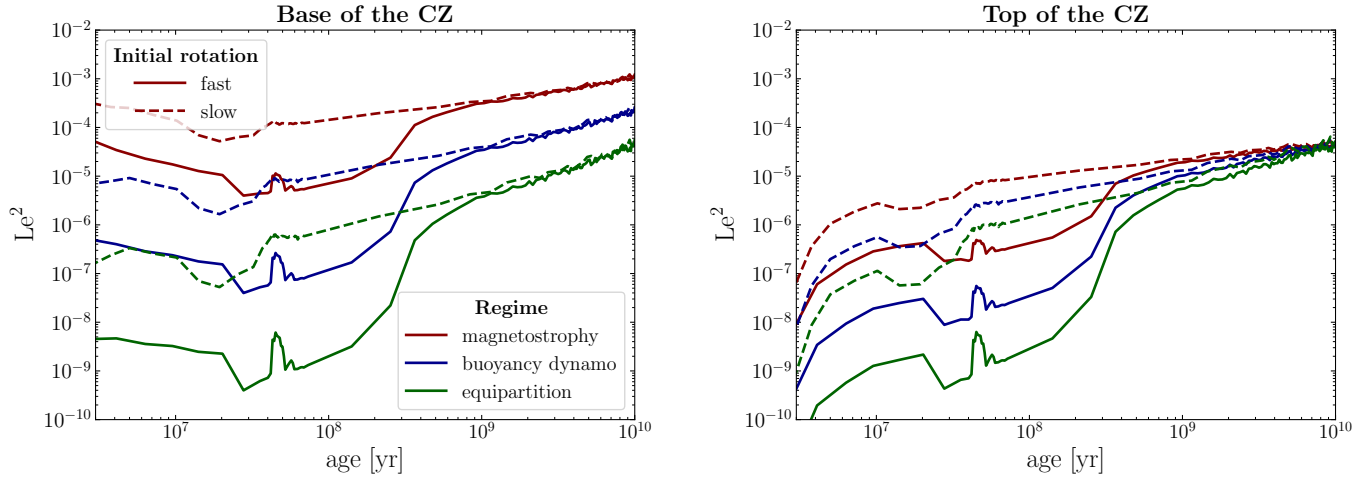


Fig. 3. Lehnert number squared at the base (*left panel*) and the top (*right panel*) of the CZ as a function of age for a 1 $M_\odot$ star, and for different magnetic scaling laws and initial rotations (see the legends in the *left panel*).

number of pairs (m, n) because the tidal potential components are labelled by these integers and depend on eccentricity and stellar obliquity. Moreover, the dominant term in the tidal potential is the quadrupolar component as long as the planet and its host star are well separated, namely $l = 2$ with l the degree of the spherical harmonics (Mathis & Le Poncin-Lafitte 2009; Ogilvie 2014). Within this assumption and the limits of low eccentricity and obliquity, $(m, n) \in \{(2, 2), (0, 1), (2, 1), (2, 3), (1, 0), (1, 2)\}$ (see Ogilvie 2014, for more mathematical details). When the orbit is strictly circularised and coplanar, the asynchronous tide acts alone and the only matching pair of integers is $(2, 2)$. For the other pairs, the eccentricity or obliquity tides can be dominant.

In Table B.1, we have thus listed known star-planet systems satisfying the following conditions:

– a near-circular orbit: we choose the eccentricity such as $e < 0.1$.

– a low sky-projected obliquity: $|\lambda| < 30°$. λ is the sky-projected angle between the stellar spin axis and the axis perpendicular to the planet orbit. Ideally, we should use the true obliquity ψ but this quantity is more difficult to determine than λ and too few measurements exist. However, when both values of ψ and λ exist for the selected systems, they are quite similar and far from the threshold of 30°.

– a planet orbiting close to its host star: $P_o < 10$ days, where P_o is the orbital period of the planet, so that stellar tidal effects are important.

Under these conditions the chosen systems are mostly hot-Jupiter-like systems, with host stars ranging from 0.7 to 1.4 $M_\odot$ in order to have a similar structure to that of the Sun (namely with a convective envelope and a radiative region below it during the MS). They have been picked out using the Extrasolar Planets Encyclopaedia[1] (e.g. Schneider et al. 2011) which presents the orbital period and eccentricity of the planet, along with the TEPcat[2] (Southworth 2011) database to find the sky-projected obliquity. Then, we removed the systems for which the age of the star was not known. For the remaining systems, stellar period has been found in the literature: the related references are reported in the last column of Table B.1.

In Fig. 5, we present the ratio of the magnetic to hydrodynamic forcings $f_{mag}/f_{hydro} = \mathrm{Le}^2\mathrm{Ro}_t^{-1}\hat{\sigma}_{max}^{-1}$ as a function of

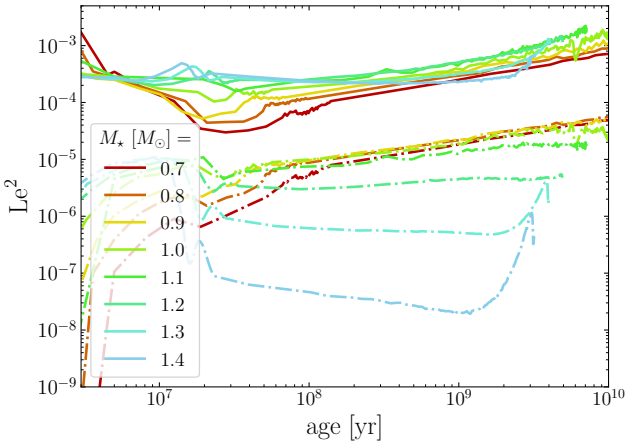


Fig. 4. Evolution of the Lehnert number squared over time, at the base (solid lines) and the top (dotted dashed lines) of the CZ, for various low-mass stars sorted from 0.7 to 1.4 $M_\odot$. Slow initial rotation has been used here and a magnetostrophic balance has been assumed.

the mass of the host star. The quantity $\mathrm{Ro}_t\hat{\sigma}_{max}$ has been calculated using orbital and stellar rotation periods (see Table B.1) for the pair (m, n) that minimises this quantity and thus maximises f_{mag}/f_{hydro}. To calculate the Lehnert number squared, we have used the star's rotation period and radius displayed in Table B.1, coupled with density, convective length and velocity given by our grid of STAREVOL models at the closest age and mass of the host star. For each system, Le^2 is evaluated at the base and the top of the CZ. Moreover, the magnetostrophic regime has been selected because it best reproduces the observed surface magnetic fields (see Figs. 1 and 2). As expected, the ratio f_{mag}/f_{hydro} at the base is greater than at the top of the CZ, consistent with the relative magnitude of the large-scale magnetic field inside the convective envelope. Moreover, at the base of the CZ the higher the mass, the greater this ratio. On the contrary, we observe a drop in f_{mag}/f_{hydro} at the top of the CZ for stars more massive than 1.2 $M_\odot$, similar to what we notice in Fig. 4. More importantly, we point out that f_{mag}/f_{hydro} is always smaller than unity, regardless of the mass of star and the position inside the stellar envelope. Only HAT-P-24 (b) may feature the ratio of forcings around unity within the error bar for $(m, n) = (2, 1)$ at the base of the CZ. Indeed, the rotation period of the star HAT-P-24 is nearly

[1] http://www.exoplanet.eu
[2] www.astro.keele.ac.uk/jkt/tepcat/tepcat.html

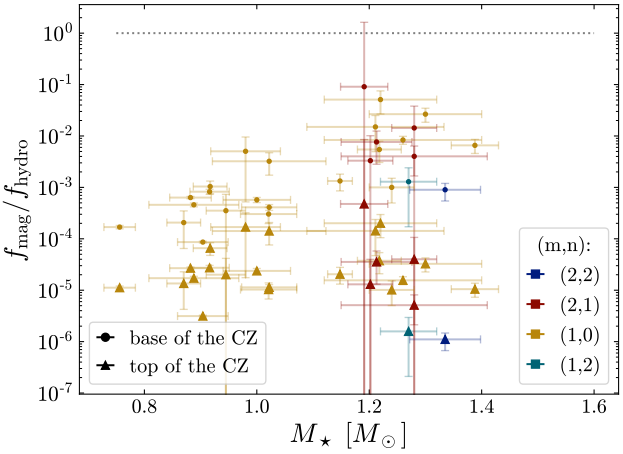


Fig. 5. Dependence of the ratio of the Lorentz forcing relative to the hydrodynamic forcing with respect to the mass of the host star for the selected star-planet systems (see Table B.1). The magnetic forcing term $f_{\rm mag}$ is estimated with the magnetostrophic balance at the base and the top of the CZ and a stellar model evolved with a slow initial rotation. The tidal frequency has been calculated with the pair (m, n) that minimises $\mathrm{Ro_t}\hat{\sigma}_{\rm max}$ and thus maximises $f_{\rm mag}/f_{\rm hydro}$.

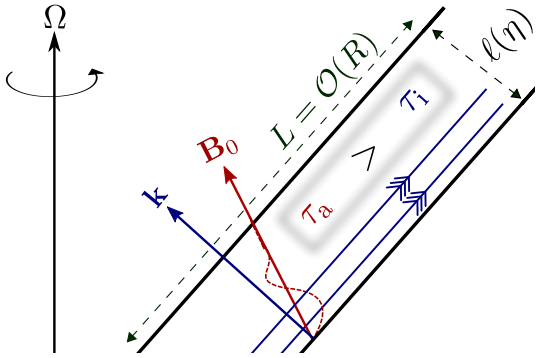


Fig. 6. Sketch of an inertial wave beam with a magnetic field (red arrow), an Alfvén wave (dashed red line) and an inertial wave propagating from the left to the right (blue arrows). The time for an Alfvén wave to transversely cross the wave beam of length $\ell(\tau_i = \tau_\eta)$, is greater than the time for an inertial wave to go through the wave beam of length $L \sim R$.

twice the orbital period of the planet HAT-P-24 b, which implies that $\mathrm{Ro_t}$ is very close to zero, thereby making $f_{\rm mag}/f_{\rm hydro}$ close to unity, despite the small value of Le^2. It is worth noticing that Ogilvie (2009) and Lin & Ogilvie (2018) mentioned a significant impact of the magnetic field on non-wave like motions as soon as $\mathrm{Le} > 0.1$. In our study, some star-planet systems (like HAT-P-13 and HD 149026) feature a Lehnert number greater than 10^{-1} and yet a ratio $f_{\rm mag}/f_{\rm hydro}$ far below unity. This stresses the fact that the Lehnert number is not the only quantity to come into play and that the relative amplitude of the tidal and rotation frequencies has to be considered to conclude on the impact of magnetism on the tidal forcing.

From the results of this section, we conclude that the tidal forcing arising from the Lorentz force remains small in comparison to a pure hydrodynamical forcing. This conclusion is important, as it stresses that adopting a Coriolis-driven tidal forcing is justified to study the propagation and dissipation of tidally-forced magneto-inertial waves in the convective envelope of low-mass stars, despite the presence of a large-scale, dynamo generated magnetic field, as was done in Wei (2016, 2018) and Lin & Ogilvie (2018).

3. The relative importance of viscous over Ohmic dissipation for magneto-inertial waves

In the previous section, we have demonstrated that the Lorentz force has a weak contribution to the tidal forcing of (magneto-) inertial waves. It can, however, affect their propagation (hence the name magneto-inertial waves) and dissipation as the Lorentz force acts on the wave-like part of the equation of motion and we have introduced the Ohmic diffusion in the induction equation (see Eqs. (5) and (4b), respectively). Wei (2016) studied the dissipation of these waves by turbulent friction and magnetic diffusion processes using a local Cartesian model of an isentropic convective region. He compared the importance of Ohmic versus viscous dissipations, especially at resonances. Varying the Lehnert number, Wei (2016) found that the transition from a viscous-dominated regime to a regime dominated by Ohmic dissipation occurs when the Lehnert number is greater than $\sim 10^{-4}$–10^{-3}, for average atomic Ekman and Prandtl numbers close to those expected in the Sun or in Jupiter. This led him to the conclusion that when Le is larger than 10^{-3}, magnetic effects on tidal dissipation should be taken into account.

This work has been taken up by Lin & Ogilvie (2018) in which they studied the propagation and the kinetic and magnetic energy dissipations of tidally forced magneto-inertial waves in a spherical shell. They showed that, at high Lehnert numbers, dissipation is no longer focused along the shear layers that are shaped by rotation and viscosity following attractors of characteristics as in the pure hydrodynamical case. Once again, they identified a critical Lehnert number that separates the regimes dominated by viscosity or by Ohmic dissipation. They expressed this critical Lehnert number with the help of characteristic timescales of ray tracing. Specifically, the width of an inertial wave beam ℓ is deduced by equating the magnetic diffusion timescale $\tau_\eta = \ell^2/\eta$ and the inertial wave propagation time $\tau_i = R/|\boldsymbol{V}_{\rm g}|$, where $|\boldsymbol{V}_{\rm g}| \sim \ell\Omega$ is the group velocity (see Fig. 6). Indeed, the higher the Ohmic diffusion (or the viscosity), the larger the spread of the inertial wave beam. Furthermore, hydrodynamical terms prevail over MHD ones when Alfvén waves (produced by the deformation of the magnetic field by the inertial flow) do not have time to distort the wave beam. In other words the hydrodynamical terms dominate when $\tau_{\rm a} > \tau_i$ where

$$\tau_{\rm a} = \ell/|\boldsymbol{V}_{\rm a}| \sim \mathrm{Le}^{-1}\Omega^{-1}\ell/R,$$

is the typical time for an Alfvén wave to transversely cross the wave beam (see Fig. 6). Using these heuristic considerations, Lin & Ogilvie (2018) have shown that the propagation of inertial waves is little influenced by a magnetic field as long as

$$\mathrm{Le} \ll \mathrm{Em}^{2/3},$$

with $\mathrm{Em} = \eta/(2\Omega R^2)$ the magnetic Ekman number. This prediction has been inferred in the context of a low Pm. This condition is generally satisfied in solar-like stars. In the Sun, the atomic magnetic Prandtl number varies from 10^{-6} at the surface to 10^{-1} at the base of the CZ (Zeldovich 1983). When viscosity dominates, for instance in the core of massive stars (see Fig. 2 in Augustson et al. 2019), the same relationship holds with the viscous Ekman number Ek instead of Em.

In Fig. 7, the Lehnert number is illustrated as a function of stellar age, where the threshold defined in Lin & Ogilvie (2018) is included with atomic and turbulent magnetic diffusivities: $\mathrm{Em}_{\rm ato}^{2/3}$ and $\mathrm{Em}_{\rm tur}^{2/3}$ being the atomic and turbulent magnetic

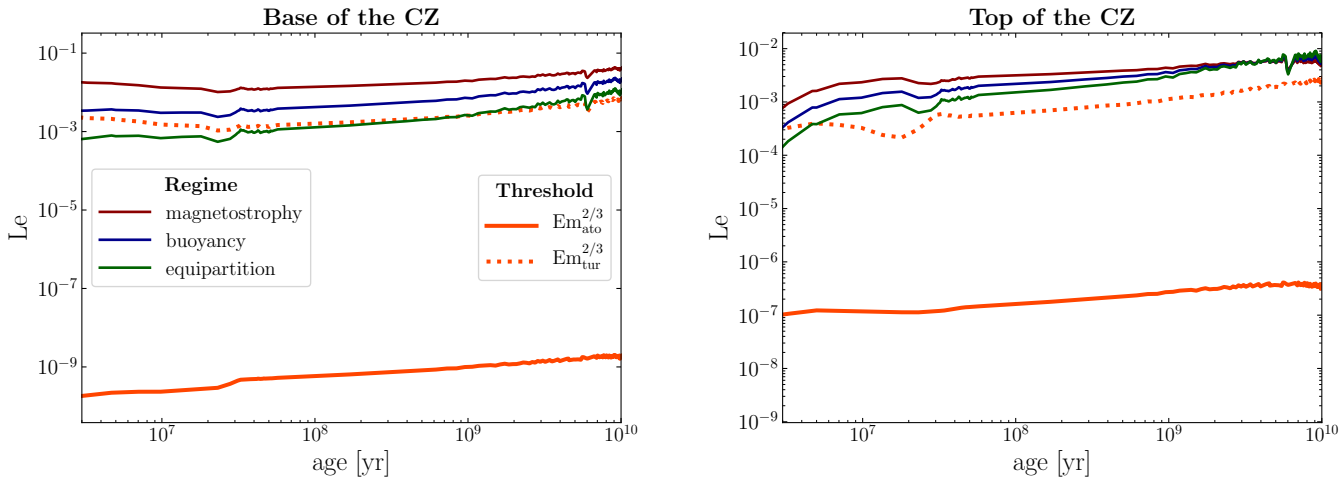


Fig. 7. Lehnert number at the base (*left panel*) and top (*right panel*) of the CZ versus the age of a 1 $M_\odot$ star. Slow initial rotation has been used in both panels. The thresholds for which magnetic field impacts the propagation of inertial waves is estimated with different Ekman numbers and drawn in orange (see the legend).

Ekman numbers, respectively. The parameter $\mathrm{Em}_{\mathrm{ato}}$ has been computed thanks to the Braginskii prescription for plasma diffusivities (Appendix B, Braginskii 1965; Augustson et al. 2019) using the grid of STAREVOL models. The turbulent magnetic Ekman number ($\mathrm{Em}_{\mathrm{tur}}$) is derived assuming that the eddy-magnetic diffusivity takes the simple form: $\eta_{\mathrm{tur}} = u_{\mathrm{c}} l_{\mathrm{c}}/3$. In this approach, η_{tur} is equivalent to the eddy-viscosity that means a magnetic turbulent Prandtl number of the order of unity (see e.g. Camargo & Tasso 1992). We highlight that in both panels of Fig. 7, the threshold calculated with an atomic magnetic diffusivity is much lower than Le derived in the various regimes, by at least three order of magnitudes near the surface and six order of magnitude at the base of the CZ. Consequently, the Ohmic dissipation largely outbalances the viscous dissipation along the lifetime of a 1 $M_\odot$ when taking Lin and Ogilvie's threshold assessed with a magnetic atomic diffusivity η_{ato}. In contrast, the limit estimated with the turbulent magnetic Ekman number is of the same order of magnitude as the Lehnert number in the equipartition regime at the base of the CZ, whereas the threshold is slightly smaller than the Lehnert number curves at the top. Note that the turbulent magnetic Ekman number is close to the value of the magnetic Ekman number used in Lin & Ogilvie's (previously quoted) paper for their simulations. This explains why the transition from an hydrodynamical to a fully magnetic regime is carried out at similar Lehnert number in their case and in ours when using $\mathrm{Em}_{\mathrm{tur}}$ here (see Figs. 2–4 in Lin & Ogilvie 2018). By choosing an eddy-magnetic diffusivity, both Ohmic and viscous dissipations have to be taken into account in the dissipation calculation.

4. The impact of a smaller-scale magnetic field

The stellar dynamo is a multi-scale process. Indeed, large-scale and small-scale dynamos coexist inside a star's CZ and produce magnetic fields at different length scales (Brandenburg & Subramanian 2005; Strugarek et al. 2013, and references therein). At the base of the CZ, the convective length scale computed by STAREVOL is about one tenth of the radius of the star and decreases drastically towards the top of the CZ ($\sim 10^{-4}\,R$ in our model). In Sect. 2.2, we have made the assumption that a dynamo-like magnetic field is the result of turbulent convective motions featured by the convective velocity at the base of the CZ, associated to a relatively large-scale convective length. Then, we have used this dynamo-induced magnetic field to extrapolate a dipolar magnetic field near the surface of the star (see Eq. (10)). However, one can question the role of the small-scale dynamo fields on tidal excitation and dissipation throughout the convective envelope.

The dynamical tides will possibly interact with the smaller-scale magnetic field. Indeed, the scale of variation of dynamical tides along the inertial wave beam is of order R (Sect. 3), but the transverse length scale l of this beam is smaller. The balance between magnetic diffusion and inertial timescales (see also Sect. 3) leads to $l = \sqrt[3]{\mathrm{Em}}\,R$ i.e. the transverse length scale of the beam varies from one hundredth to one tenth of the stellar radius when using typical values of the turbulent Ekman number (see Fig. 7). This orthogonal length scale is thus comparable to the length scale of the convection and of the corresponding magnetic field.

The scale of variation of the equilibrium tide is also of order R (see e.g. Remus et al. 2012). The small-scale components of the star's magnetic field can collectively affect the large-scale flow of the equilibrium tide provided their correlations sustain a large-scale effective Lorentz force. We plot Le^2 associated with a small-scale magnetic field in Fig. 8 as a function of the normalised radius in the whole CZ. The typical length to be used in the expression of f_{mag} (Eq. (6)) is no longer R but l_{c} which represents the characteristic length of the fluctuating component of the dynamo-generated magnetic field. We redefine the Lehnert number here as $\mathrm{Le} = B_{\mathrm{dyn}}/(\sqrt{\mu_0\rho}2\Omega l_{\mathrm{c}})$, where B_{dyn} (Table 1) depends upon l_{c}, which in turn varies inside the CZ. In the three regimes listed in Table 2, Le now depends only on the Rossby number (i.e. each scaling has to be multiplied by R/l_{c}). The profile of Le^2 is shown for magnetostrophic and equipartition regimes at different evolutionary stages. In both regimes, the Lehnert number follows the Rossby number tendency obtained in Mathis et al. (2016). Indeed, the authors pointed out that Ro always increases with radius, regardless of the changes in mass and stellar evolutionary phases. In the early stages of the 1 $M_\odot$ star's evolution (PMS and ZAMS), the probability of having a significant magnetic forcing e.g. $f_{\mathrm{mag}}/f_{\mathrm{hydro}} > 1$ is weak at the base of the CZ ($\mathrm{Le}^2 < 10^{-3}$), but becomes high near the surface ($\mathrm{Le}^2 > 10$) based on the analyses of Sects. 2.5 and 2.6. The chances are even higher when the star is older (from the midpoint

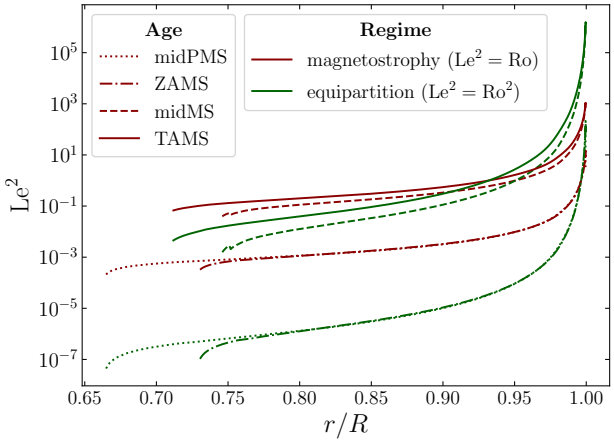


Fig. 8. Lehnert number squared against the normalised radius in the magnetostrophic (dark red) and equipartition (green) regimes, for a 1 $M_\odot$ star. The reader is referred to the body of Sect. 4 for the new definition of Le that involves a small-scale magnetic field. The Lehnert number squared is plotted at different epochs: amid the pre-main sequence (midPMS; ~30 Myr), at zero-age main sequence (ZAMS; ~60 Myr), amid the main sequence (midMS; ~5.3 Gyr), and toward the end of the main sequence (TAMS; ~10.5 Gyr).

to the end of the MS) since Le^2 is already greater than 10^{-3} at the base of the CZ in both regimes.

From this analysis, we should keep in mind that small-scale magnetic fields can affect the equilibrium and dynamical tides. Indeed, Le^2 can be significantly enhanced near the surface of the star, a fortiori for all three regimes described in Table 1. This may change the results of Sect. 2.6, namely boost the effect of magnetism on tidal forcing so that $f_{\rm mag}$ is no longer negligible in front of $f_{\rm hydro}$.

5. Conclusions and discussions

The influence of magnetism on tidal interaction along the evolution of low-mass stars has been investigated through its impact on tidal excitation and dissipation. We have first derived an analytic criterion to quantify the Lorentz contribution to the tidal forcing. The relative importance of Coriolis-like versus Lorentz-like forcings relies on the Lehnert number and characteristic frequencies of star-planet systems, i.e. the tidal frequency and the rotation frequency of the main body. With the help of simple scaling laws, we have estimated the magnitude of a dynamo-generated magnetic field near the tachocline. Then, a large-scale dipolar magnetic field has been inferred near the surface of the star from these scaling relationships. For this purpose, we have used grids of low-mass stars computed by the stellar evolution code STAREVOL (Amard et al. 2019). This allowed us to compare our magnetic field estimates at the surface with the observations of the surface dipolar magnetic field. We find that the magnetostrophic regime (resulting from the balance between Coriolis and Lorentz forces) gives a good estimate, within an order of magnitude, of the magnetic fields of PMS and MS stars when assuming a median or fast initial rotation. Nevertheless, improvements still need to be made in terms of magnetic scaling laws in order to better reproduce the observed magnetic fields of Vidotto et al. (2014) and See et al. (2017) (see Appendix B).

Subsequently, we have estimated the Lehnert number with these prescriptions for the stellar dynamo at the base and the top of the CZ. We have explored how it varies for different stellar masses and initial rotation speeds as a function of time. In all cases, the Lehnert number is small compared to unity. This means that magnetism can play a role in tidal forcing only for small tidal to rotational frequency ratios. In practice, this condition is verified neither at the base nor at the top of the CZ when using the large-scale magnetic fields in the primary component of quasi-circular and coplanar star-planet systems. Although the ratio $f_{\rm mag}/f_{\rm hydro}$ increases with the mass of the host star until 1.2 $M_\odot$ (see Fig. 5) and is greater at the base of the CZ, it remains below 1 for all the studied systems. Indeed, only specific and sharp enough resonances between the tidal and the rotational frequency can increase the $f_{\rm mag}/f_{\rm hydro}$ ratio. This statement is also valid for non-circular and non-coplanar systems, the tidal frequency being just a different combination of orbital and rotation frequencies. Eventually, one should note that all the selected systems (Table B.1) have a host star on the mid and late MS. But it should not change the fact that large-scale magnetic fields have little influence on the tidal excitation because Le^2 is even weaker for younger stars (as we have seen in Fig. 4).

In contrast, the dissipation of the dynamical tide is strongly affected by stellar magnetism. Indeed, we have shown that viscous dissipation is no longer the main process of energy dissipation. Ohmic dissipation is at least as important as viscous dissipation (see Fig. 7) in the whole CZ for a 1$M_\odot$ star as well as other low-mass stars. This means that a full MHD treatment is needed to analyse the propagation and dissipation of tidally-forced (magneto-) inertial waves inside the CZ of a low-mass star.

It can be added that whatever the energy mix distributed in the toroidal and poloidal components of the large-scale magnetic field at the surface (which is also variable over time Kochukhov et al. 2017), it does not change the main conclusions of our paper because these energies are comparable within an order of magnitude (See et al. 2015).

In Sect. 4, we have addressed the question of the effect of small-scale components of the dynamo-induced magnetic field on tidal interactions. We have pointed out that they are likely to play a role on both dynamical and equilibrium tides and consequently on the tidal forcing and dissipation. We first demonstrated that the transverse component of the typical length scale of the dynamical tide is commensurate with the convective mixing length in the bulk of the CZ. In this respect, it would also mean that the modelling of the friction applied by turbulent convection on the dynamical tides should go beyond an eddy viscosity model (Ogilvie & Lesur 2012) to incorporate magnetic effects. Then, we showed that the Lehnert number squared estimated with a small-scale magnetic field can be much greater than Le^2 calculated with a large-scale field. As a result, the impact of a small-scale dynamo induced magnetic field on tidal forcing could be not as negligible as the effect of a larger-scale magnetic field. Quantifying this impact now requires ab-initio modelling of tidal forcing in turbulent convective envelopes sustaining a small-scale dynamo.

Acknowledgements. We would like to thank the anonymous referee for the helpful comments and suggestions regarding our work. A. Astoul, K. Augustson, E. Bolmont, and S. Mathis acknowledge funding by the European Research Council through the ERC grant SPIRE 647383. The authors acknowledge the PLATO CNES funding at CEA/IRFU/DAp and IRAP. The authors further thank V. See for fruitful discussions and the use of his data. F. Gallet acknowledges financial support from a CNES fellowship. A. S. Brun acknowledges funding by ERC WHOLESUN 810218 grant, INSU/PNST, and CNES Solar Orbiter. This work has been carried out within the framework of the NCCR PlanetS supported by the Swiss National Science Foundation. This research has made use of NASA's Astrophysics Data System.

References

Amard, L., Palacios, A., Charbonnel, C., Gallet, F., & Bouvier, J. 2016, A&A, 587, A105
Amard, L., Palacios, A., Charbonnel, C., et al. 2019, A&A, 631, A77
Anderson, D. R., Barros, S. C. C., Boisse, I., et al. 2011, PASP, 123, 555
Anderson, D. R., Brown, D. J. A., Collier Cameron, A., et al. 2014, MNRAS, submitted [arXiv:1410.3449]
Antia, H. M., Chitre, S. M., & Thompson, M. J. 2000, A&A, 360, 335
Asplund, M., Grevesse, N., Sauval, A. J., & Scott, P. 2009, ARA&A, 47, 481
Augustson, K. C., Brun, A. S., & Toomre, J. 2019, ApJ, 876, 83
Barker, A. J., & Ogilvie, G. I. 2010, MNRAS, 404, 1849
Basu, S. 2016, Liv. Rev. Sol. Phys., 13, 2
Beck, P. G., Mathis, S., Gallet, F., et al. 2018, MNRAS, 479, L123
Bell, C. P. M., Naylor, T., Mayne, N. J., Jeffries, R. D., & Littlefair, S. P. 2013, MNRAS, 434, 806
Benbakoura, M., Réville, V., Brun, A. S., Le Poncin-Lafitte, C., & Mathis, S. 2019, A&A, 621, A124
Bolmont, E., Gallet, F., Mathis, S., et al. 2017, A&A, 604, A113
Bolmont, E., & Mathis, S. 2016, Celest. Mech. Dyn. Astron., 126, 275
Braginskii, S. I. 1965, Rev. Plasma Phys., 1, 205
Brandenburg, A., & Subramanian, K. 2005, Phys. Rep., 417, 1
Brown, D. J. A. 2014, MNRAS, 442, 1844
Brun, A. S., & Browning, M. K. 2017, Liv. Rev. Sol. Phys., 14, 4
Brun, A. S., García, R. A., Houdek, G., Nandy, D., & Pinsonneault, M. 2015, Space Sci. Rev., 196, 303
Camargo, S. J., & Tasso, H. 1992, Phys. Fluids B, 4, 1199
Charbonneau, P. 2013, Solar and Stellar Dynamos: Saas-Fee Advanced Course 39 Swiss Society for Astrophysics and Astronomy (Springer-Verlag: Berlin, Heidelberg), 39
Charbonneau, P. 2014, ARA&A, 52, 251
Christensen, U. R., Holzwarth, V., & Reiners, A. 2009, Nature, 457, 167
Cowling, T. G. 1941, MNRAS, 101, 367
Czesla, S., Salz, M., Schneider, P. C., Mittag, M., & Schmitt, J. H. M. M. 2017, A&A, 607, A101
Davidson, P. A. 2013, Geophys. J. Int., 195, 67
DeRosa, M. L., Brun, A. S., & Hoeksema, J. T. 2012, ApJ, 757, 96
Donati, J. F., Catala, C., Landstreet, J. D., & Petit, P. 2006, in ASP Conf. Ser., ed. R. Casini, 358, 362
Donati, J.-F., & Landstreet, J. D. 2009, ARA&A, 47, 333
Donati, J.-F., Jardine, M. M., Gregory, S. G., et al. 2007, MNRAS, 380, 1297
Duez, V., Mathis, S., & Turck-Chièze, S. 2010, MNRAS, 402, 271
Emeriau-Viard, C., & Brun, A. S. 2017, ApJ, 846, 8
Esposito, M., Covino, E., Desidera, S., et al. 2017, A&A, 601, A53
Ferraz-Mello, S., Tadeu dos Santos, M., Folonier, H., et al. 2015, ApJ, 807, 78
Finlay, C. C. 2008, in Dynamos, eds. P. Cardin, & L. Cugliandolo (Amsterdam: Elsevier), Les Houches, 88, 403
Folsom, C. P., Petit, P., Bouvier, J., et al. 2016, MNRAS, 457, 580
Gallet, F., & Bouvier, J. 2013, A&A, 556, A36
Gallet, F., & Bouvier, J. 2015, A&A, 577, A98
Gallet, F., Bolmont, E., Mathis, S., Charbonnel, C., & Amard, L. 2017, A&A, 604, A112
Gandolfi, D., Hébrard, G., Alonso, R., et al. 2010, A&A, 524, A55
Ge, J., van Eyken, J., Mahadevan, S., et al. 2006, ApJ, 648, 683
Gilliland, R. L. 1986, ApJ, 300, 339
Goldreich, P., & Nicholson, P. D. 1989, ApJ, 342, 1079
Goodman, J., & Dickson, E. S. 1998, ApJ, 507, 938
Gough, D. O., & Thompson, M. J. 1990, MNRAS, 242, 25
Granata, V., Nascimbeni, V., Piotto, G., et al. 2014, Astron. Nachr., 335, 797
Guenel, M., Baruteau, C., Mathis, S., & Rieutord, M. 2016a, A&A, 589, A22
Guenel, M., Mathis, S., Baruteau, C., & Rieutord, M. 2016b, ArXiv e-prints [arXiv:1612.05071]
Hébrard, G., Collier Cameron, A., Brown, D. J. A., et al. 2013, A&A, 549, A134
Hirano, T., Sanchis-Ojeda, R., Takeda, Y., et al. 2012, ApJ, 756, 66
Hut, P. 1980, A&A, 92, 167
Janson, M., Reffert, S., Brandner, W., et al. 2008, A&A, 488, 771
Jardine, M., & Unruh, Y. C. 1999, A&A, 346, 883
Jurčišinová, E., Jurčišin, M., Remecký, R., & Zalom, P. 2013, Phys. Rev. E, 87, 043010
Käpylä, P. J., Rheinhardt, M., Brandenburg, A., & Käpylä, M. J. 2019, A&A, submitted [arXiv:1901.00787]
Kochukhov, O., Petit, P., Strassmeier, K. G., et al. 2017, Astron. Nachr., 338, 428
Lagarde, N., Decressin, T., Charbonnel, C., et al. 2012, A&A, 543, A108
Landin, N. R., Mendes, L. T. S., & Vaz, L. P. R. 2010, A&A, 510, A46
Lanza, A. F., Damiani, C., & Gandolfi, D. 2011, A&A, 529, A50
Lehnert, B. 1954, ApJ, 119, 647
Lin, Y., & Ogilvie, G. I. 2018, MNRAS, 474, 1644
Line, M. R., Teske, J., Burningham, B., Fortney, J. J., & Marley, M. S. 2015, ApJ, 807, 183
Mancini, L., Esposito, M., Covino, E., et al. 2015, A&A, 579, A136
Mancini, L., Esposito, M., Covino, E., et al. 2018, A&A, 613, A41
Mathis, S. 2015, A&A, 580, L3
Mathis, S., & Le Poncin-Lafitte, C. 2009, A&A, 497, 889
Mathis, S., Auclair-Desrotour, P., Guenel, M., Gallet, F., & Le Poncin-Lafitte, C. 2016, A&A, 592, A33
Matt, S. P., Brun, A. S., Baraffe, I., Bouvier, J., & Chabrier, G. 2015, ApJ, 799, L23
Maxted, P. F. L., Serenelli, A. M., & Southworth, J. 2015, A&A, 577, A90
Mayor, M., Queloz, D., Udry, S., & Halbwachs, J. L. 1997, in IAU Colloq. 161: Astronomical and Biochemical Origins and the Search for Life in the Universe, eds. C. Batalli Cosmovici, S. Bowyer, & D. Werthimer, 313
Mohler-Fischer, M., Mancini, L., Hartman, J. D., et al. 2013, A&A, 558, A55
Ogilvie, G. I. 2005, J. Fluid Mech., 543, 19
Ogilvie, G. I. 2009, MNRAS, 396, 794
Ogilvie, G. I. 2013, MNRAS, 429, 613
Ogilvie, G. I. 2014, ARA&A, 52, 171
Ogilvie, G. I., & Lesur, G. 2012, MNRAS, 422, 1975
Ogilvie, G. I., & Lin, D. N. C. 2004, ApJ, 610, 477
Ogilvie, G. I., & Lin, D. N. C. 2007, ApJ, 661, 1180
Perryman, M. 2018, The Exoplanet Handbook (Cambridge: Cambridge University Press)
Rebull, L. M., Wolff, S. C., & Strom, S. E. 2004, AJ, 127, 1029
Reiners, A. 2012, Liv. Rev. Sol. Phys., 9, 1
Remus, F., Mathis, S., & Zahn, J. P. 2012, A&A, 544, A132
Schlichting, H. E. 2014, ApJ, 795, L15
Schneider, J., Dedieu, C., Le Sidaner, P., Savalle, R., & Zolotukhin, I. 2011, A&A, 532, A79
See, V., Jardine, M., Vidotto, A. A., et al. 2015, MNRAS, 453, 4301
See, V., Jardine, M., Vidotto, A. A., et al. 2017, MNRAS, 466, 1542
See, V., Matt, S. P., Folsom, C. P., et al. 2019, ApJ, 876, 118
Skumanich, A. 1972, ApJ, 171, 565
Southworth, J. 2011, MNRAS, 417, 2166
Spiegel, E. A., & Zahn, J. P. 1992, A&A, 265, 106
Strugarek, A., Brun, A. S., Mathis, S., & Sarazin, Y. 2013, ApJ, 764, 189
Strugarek, A., Beaudoin, P., Charbonneau, P., Brun, A. S., & Nascimento, J. D. 2017, Science, 357, 185
Terquem, C., Papaloizou, J. C. B., Nelson, R. P., & Lin, D. N. C. 1998, ApJ, 502, 788
Tregloan-Reed, J., Southworth, J., & Tappert, C. 2013, MNRAS, 428, 3671
Tregloan-Reed, J., Southworth, J., Burgdorf, M., et al. 2015, MNRAS, 450, 1760
Vidotto, A. A., Gregory, S. G., Jardine, M., et al. 2014, MNRAS, 441, 2361
Vilhu, O. 1984, A&A, 133, 117
Weber, E. J., & Davis, Jr., L. 1967, ApJ, 148, 217
Wei, X. 2016, ApJ, 828, 30
Wei, X. 2018, ApJ, 854, 34
Winn, J. N., Noyes, R. W., Holman, M. J., et al. 2005, ApJ, 631, 1215
Witte, M. G., & Savonije, G. J. 2002, A&A, 386, 222
Wright, N. J., & Drake, J. J. 2016, Nature, 535, 526
Zahn, J. P. 1966a, Ann. Astrophys., 29, 313
Zahn, J. P. 1966b, Ann. Astrophys., 29, 489
Zahn, J. P. 1966c, Ann. Astrophys., 29, 565
Zahn, J. P. 1975, A&A, 41, 329
Zahn, J. P. 1977, A&A, 500, 121
Zahn, J. P. 1989, A&A, 220, 112
Zahn, J. P., & Bouchet, L. 1989, A&A, 223, 112
Zanni, C., & Ferreira, J. 2013, A&A, 550, A99
Zeldovich, Y. B. 1983, Magnetic Fields in Astrophysics (New York: Gordon and Breach)

Appendix A: Magnetic field scaling laws

Several estimates of the magnetic field of stars can be derived thanks to energetic or force balances in the equations for heat transport (items ii and iii below) or for momentum (items i, and also ii and iii). Based on the MHD equations, and assuming stationarity, the Navier-Stokes equation of convective motions is

$$\underbrace{2\rho\boldsymbol{\Omega}\times\boldsymbol{u}}_{(1)}+\underbrace{\rho(\boldsymbol{u}\cdot\boldsymbol{\nabla})\boldsymbol{u}}_{(2)}=-\boldsymbol{\nabla}p+\rho\nu\Delta\boldsymbol{u}+\underbrace{\frac{\boldsymbol{\nabla}\times\boldsymbol{B}}{\mu_0}\times\boldsymbol{B}}_{(3)}+\rho\mathbf{g}, \quad \text{(A.1)}$$

where we have introduced $\mathbf{g}$ the gravitational acceleration of the star. At the base of the CZ, we assume that the gradient and the velocity scale like $\nabla \approx l_c^{-1}$ and $\|\boldsymbol{u}\| \approx u_c$.

i Magnetostrophy
In this regime, the Lorentz force balances the Coriolis force i.e. (3) ≈ (1) in Eq. (A.1). Thus,

$$\frac{B^2}{\mu_0 l_c}\approx\rho 2\Omega u_c \Rightarrow B\approx\sqrt{2\mu_0\mathrm{KE}\times\mathrm{Ro}^{-1}}, \quad \text{(A.2)}$$

where $\mathrm{KE}=\rho u_c^2/2$ is the kinetic energy density associated with convective motions, and $\mathrm{Ro}=u_c/(2\Omega l_c)$ the convective Rossby number.

ii Equipartition regime
In this regime we assume that the dynamo is efficient enough such that the convective kinetic energy density KE of the fluid is equivalent to the magnetic energy density $\mathrm{ME}=B^2/(2\mu_0)$ i.e. (3) ≈ (2) in Eq. (A.1):

$$\mathrm{ME}\approx\mathrm{KE}\Rightarrow\frac{B^2}{\mu_0}\approx\rho u_c^2\Rightarrow B\approx\sqrt{2\mu_0\mathrm{KE}}. \quad \text{(A.3)}$$

iii Buoyancy dynamo
Taking the curl of Eq. (A.1) and neglecting viscous and inertial forces we obtain

$$\rho(\boldsymbol{\Omega}\cdot\boldsymbol{\nabla})\mathbf{v}=\boldsymbol{\nabla}\times\left(\frac{\boldsymbol{\nabla}\times\boldsymbol{B}}{\mu_0}\times\boldsymbol{B}\right)+\boldsymbol{\nabla}\rho\times\mathbf{g}, \quad \text{(A.4)}$$

assuming that the velocity is divergence-free. The buoyancy dynamo lies on the fact that each term in Eq. (A.4) has the same order of magnitude (Davidson 2013; Augustson et al. 2019). If the Rossby number is small enough, namely the rotation frequency of the body is larger than the convective frequency (the inverse of the convective turnover time), the convective flows become almost columnar, and aligned along the rotation axis. In the stellar evolution grids we use, this assumption is at least verified in the first half of the CZ from the base. As a consequence, two characteristic length scales appear, $l_\parallel$ and $l_\perp$: these lengths are parallel and perpendicular to the rotation axis, respectively. A direct result is that $l_\perp < l_\parallel$, and we assume that $l_c \simeq l_\parallel$ so that the convective Rossby number is now $\mathrm{Ro}=u_c/(2\Omega l_\parallel)$. It seems consistent with the high values of the convective length scale we find at the base of the envelope for different stars (several tenths as the CZ thickness). Thus, taking the characteristic scales of each quantities in Eq. (A.4):

$$\frac{\Omega u_c}{l_\parallel}\approx\frac{g}{l_\perp}\approx\frac{B^2}{\rho\mu_0 l_\perp^2}, \quad \text{(A.5)}$$

where $\boldsymbol{\Omega}\boldsymbol{\nabla}\approx\Omega/l_\parallel$ by definition of $l_\parallel$, otherwise $\nabla\propto l_\perp^{-1}$ because $l_\perp < l_\parallel$. Then, we set up $p_g = g u_c$ the buoyancy power (or rate of buoyancy work) per unit of mass. We can also express the magnetic energy in term of buoyancy power because of the equivalence of forces in Eq. (A.4). Therefore, in order to respect dimensional homogeneity, the magnetic energy per unit of mass satisfies the following relationship:

$$\frac{B^2}{\rho\mu_0}=l_\parallel^{2/3}p_g^{2/3}, \quad \text{(A.6)}$$

where we are only using $l_\parallel$, again because $l_\parallel > l_\perp$ since we are looking for the large-scale dynamo magnetic field. From the equivalences in Eq. (A.5), we can express g as a function of Ω, u_c, $l_\parallel$ and the energy by unit of mass $B^2/(\rho\mu_0)$:

$$g^2=\frac{\Omega u_c}{l_\parallel}\frac{B^2}{\rho\mu_0}. \quad \text{(A.7)}$$

Injecting Eq. (A.7) in $p_g^2=(gu_c)^2$, and all of this in Eq. (A.6), one can find:

$$\left(\frac{B^2}{\rho\mu_0}\right)^2=l_\parallel\Omega u_c^3. \quad \text{(A.8)}$$

Considering that $\mathrm{Ro}=u_c/(2\Omega l_\parallel)$, Eq. (A.8) can be written finally in the form:

$$\frac{\mathrm{ME}}{\mathrm{KE}}=\mathrm{Ro}^{-1/2}, \text{or } B=\sqrt{2\mu_0\mathrm{KE}\times\mathrm{Ro}^{-1/2}}. \quad \text{(A.9)}$$

Appendix B: Limitations of the best scaling for B_{dip}^{obs}

In Figs. 1 and 2, we observe that B_{dip} calculated with the magnetostrophic regime and a fast initial rotation at the top of the CZ is in adequacy with the observed dipolar magnetic field at the surface. We present here some limitations of this comparison. In Fig. B.1, we display the angular velocity (and the period in the vertical right axis) of the 0.9 $M_\odot$ stars featured in Fig. 1 against their age, compared to the different rotational evolutions given by STAREVOL. The angular velocities are found in See et al. (2017) and references therein. They are obtained mainly through photometry while the age of the stars are mostly determined by the comparison between isochrones and colour-magnitude diagrams. Note that the error bars of the angular velocities are too small to be visible on the graph. We point out that the rotation periods of the stars seem to be in agreement with the slow or median rotation profiles provided by STAREVOL, unlike what we observed for the surface dipolar magnetic fields in Fig. 1. To some extent, the same assessment is made when displaying rotation versus time diagram for other low-mass stars (not presented here). There are several possible explanations for this result. The discrepancy could be first attributed to the simplicity of our dynamo-induced magnetic fields models. Then, it is possible that the metallicity affects the rotation evolution models as it has been demonstrated by Amard et al. (in prep.) (we remind the reader that the metallicity is fixed in Sect. 2.3 to the solar value). Furthermore, as we said in Sect. 2.4, this observation tends to be more nuanced with increasing data. As a result, we have to cautiously interpret the fact that B_{dip} estimated with the magnetostrophic regime and a fast initial rotation match the observed values of the dipolar magnetic field at the surface.

Table B.1. Star-planet systems with a quasi-circular and quasi-coplanar orbit, $e < 0.1$ and $|\lambda| < 30°$ with e and λ the eccentricity and the sky-projected spin-orbit misalignment angle, respectively.

Systems	$M_\star$ [$M_\odot$]	age [Gyr]	R [$R_\odot$]	P_o [d]	$P_\star$ [d]	References
CoRoT-11 (b)	1.27 ± 0.05	2.0 ± 1.0	1.43 ± 0.033	$2.994325 \pm 2.1 \times 10^{-5}$	1.73 ± 0.22	1
HAT-P-3 (b)	0.917 ± 0.03	1.6 ± 1.3	0.827 ± 0.055	$2.899703 \pm 5.4 \times 10^{-5}$	20.2 ± 2.0	2
HAT-P-4 (b)	1.26 ± 0.14	$4.2^{+2.6}_{-0.6}$	1.27 ± 0.05	$3.0565114 \pm 2.8 \times 10^{-6}$	$14.0^{+1.0}_{-0.9}$	3
HAT-P-8 (b)	1.28 ± 0.04	3.4 ± 1.0	1.5 ± 0.06	$3.0763402 \pm 1.5 \times 10^{-6}$	$5.9^{+0.5}_{-0.4}$	3
HAT-P-9 (b)	1.28 ± 0.13	1.6 ± 1.4	1.4 ± 0.06	$3.922814 \pm 2 \times 10^{-6}$	5.61 ± 0.78	4
HAT-P-13 (b)	1.22 ± 0.1	5.0 ± 0.8	1.28 ± 0.079	$2.916243 \pm 3 \times 10^{-6}$	$47.4^{+14.1}_{-8.9}$	3
HAT-P-16 (b)	1.218 ± 0.039	2.0 ± 0.8	1.289 ± 0.066	$2.77596 \pm 3 \times 10^{-6}$	$16.0^{+4.1}_{-2.8}$	3
HAT-P-20 (b)	0.756 ± 0.028	6.7 ± 3.8	0.867 ± 0.033	$2.875317 \pm 4 \times 10^{-6}$	14.48 ± 0.02	5, 6
HAT-P-22 (b)	0.916 ± 0.035	12.4 ± 2.6	1.08 ± 0.058	$3.21222 \pm 9 \times 10^{-6}$	28.7 ± 0.4	2
HAT-P-24 (b)	1.191 ± 0.042	2.8 ± 0.6	1.242 ± 0.067	$3.35524 \pm 7 \times 10^{-6}$	6.67 ± 0.68	4
HAT-P-27 (b)	0.945 ± 0.035	4.4 ± 2.6	1.055 ± 0.036	$3.0395803 \pm 1.5 \times 10^{-6}$	17.8 ± 7.8	7
HAT-P-36 (b)	1.022 ± 0.049	6.6 ± 1.8	1.264 ± 0.071	$1.327347 \pm 3 \times 10^{-6}$	15.3 ± 0.4	8
HATS-2 (b)	0.882 ± 0.037	9.7 ± 2.9	1.168 ± 0.03	$1.354133 \pm 1 \times 10^{-6}$	24.98 ± 0.04	9, 10
HD 149026 (b)	1.3 ± 0.1	2.0 ± 0.8	0.718 ± 0.065	$2.8758916 \pm 1.4 \times 10^{-6}$	$10.0^{+1.2}_{-1.0}$	3
HD 209458 (b)	1.148 ± 0.022	4.0 ± 2.0	1.38 ± 0.018	$3.52472 \pm 2.82 \times 10^{-5}$	14.4 ± 2.1	20, 21
KELT-1 (b)	1.335 ± 0.063	1.75 ± 0.25	$1.15^{+0.1}_{-0.16}$	$1.217514 \pm 1.5 \times 10^{-5}$	1.35 ± 0.04	11
Kepler-8 (b)	1.213 ± 0.063	3.84 ± 1.5	1.419 ± 0.058	$3.52254 \pm 5 \times 10^{-5}$	7.5 ± 0.3	12
TrES-2 (b)	0.98 ± 0.062	5.1 ± 2.7	1.189 ± 0.025	$2.4706133738 \pm 1.87 \times 10^{-8}$	$48.7^{+56.0}_{-17.8}$	3
TrES-4 (b)	1.388 ± 0.042	2.9 ± 0.3	1.706 ± 0.056	$3.5539268 \pm 3.2 \times 10^{-6}$	$10.7^{+1.7}_{-1.3}$	3
WASP-5 (b)	1.0 ± 0.06	3.0 ± 1.4	1.171 ± 0.057	$1.6284246 \pm 1.3 \times 10^{-6}$	16.2 ± 0.4	9
WASP-6 (b)	0.888 ± 0.08	11.0 ± 7.0	$1.224^{+0.051}_{-0.052}$	$3.361006 \pm 3.5 \times 10^{-6}$	23.8 ± 0.15	15
WASP-14 (b)	1.211 ± 0.122	0.75 ± 0.25	$1.281^{+0.075}_{-0.082}$	$2.2437661 \pm 1.1 \times 10^{-6}$	23.68 ± 6.35	4
WASP-16 (b)	1.022 ± 0.101	2.3 ± 2.2	1.008 ± 0.071	$3.1186009 \pm 1.31 \times 10^{-5}$	$33.8^{+8.9}_{-6.1}$	3
WASP-18 (b)	1.24 ± 0.04	0.63 ± 0.53	1.165 ± 0.077	$0.9414518 \pm 4 \times 10^{-7}$	5.6 ± 1.11	4
WASP-19 (b)	0.904 ± 0.045	11.5 ± 2.7	1.395 ± 0.025	$0.78884 \pm 3 \times 10^{-7}$	11.76 ± 0.09	9, 16
WASP-20 (b)	1.202 ± 0.04	$7.0^{+1.0}_{-2.0}$	1.459 ± 0.057	$4.8996285 \pm 3.4 \times 10^{-6}$	$8.1^{+3.0}_{-2.7}$	3
WASP-28 (b)	1.021 ± 0.05	$5.0^{+2.0}_{-3.0}$	1.213 ± 0.042	$3.40883 \pm 6 \times 10^{-6}$	$13.0^{+2.3}_{-1.8}$	3
WASP-52 (b)	0.87 ± 0.03	0.4 ± 0.3	1.27 ± 0.03	$1.7497798 \pm 1.2 \times 10^{-6}$	11.8 ± 3.3	18
WASP-111 (b)	1.5 ± 0.11	2.6 ± 0.6	1.442 ± 0.094	$2.310965 \pm 3.4 \times 10^{-6}$	8.4 ± 0.7	19

Notes. All the planets are hot Jupiters, denoted (b), and characterised by an orbital period P_o found in the http://exoplanet.eu/ catalogue, along with the age, the radius R, and the mass $M_\star$ of the host star. The errors of these parameters (coming from the catalogue) generally refer to 1σ errors (Schneider et al. 2011). The references are for the stellar rotation period $P_\star$.

References. (1) Gandolfi et al. (2010); (2) Mancini et al. (2018); (3) Brown (2014); (4) Lanza et al. (2011); (5) Esposito et al. (2017); (6) Granata et al. (2014); (7) Anderson et al. (2011); (8) Mancini et al. (2015); (9) Maxted et al. (2015); (10) Mohler-Fischer et al. (2013); (11) Ferraz-Mello et al. (2015); (12) Hirano et al. (2012); (15) Tregloan-Reed et al. (2015); (16) Tregloan-Reed et al. (2013); (18) Hébrard et al. (2013); (19) Anderson et al. (2014); (20) Winn et al. (2005); (21) Czesla et al. (2017).

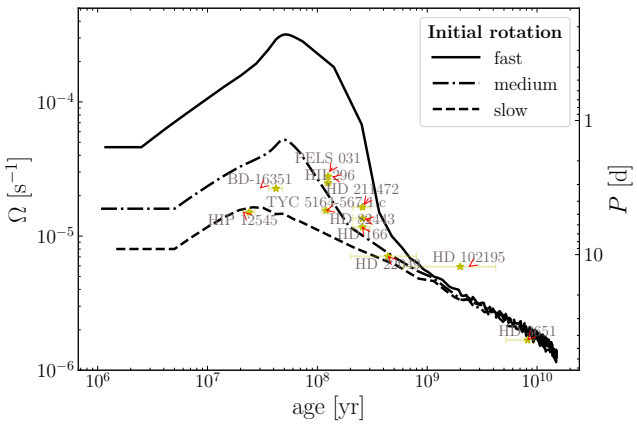


Fig. B.1. Rotation frequency on the vertical left axis (and period on the vertical right axis) versus the age of 0.9 $M_\odot$ stars (★), given fast, median, and slow initial rotations. Ages, stellar periods and their associated error bars can be found in the papers quoted in Fig. 1.